Cell Reports
Medicine

Article

Single-cell spatial analysis stratifies lung adenocarcinoma with rare actionable mutations and reveals immune-modulatory cellular crosstalk

Graphical abstract

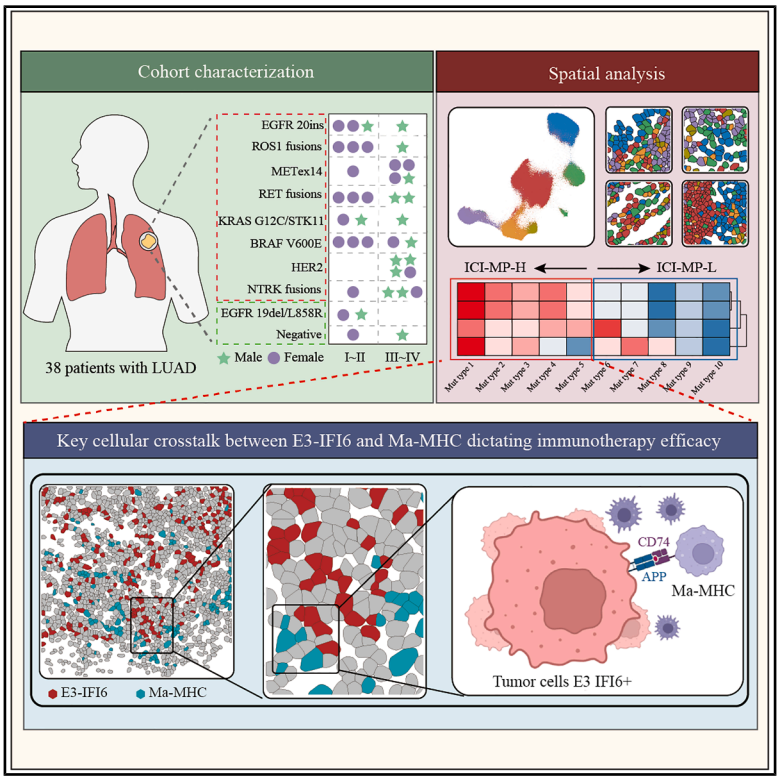

Highlights

- LUAD with rare oncogenes are stratified into two groups by ICI response signatures
- The ICI-MP-H group enriches an interferon-responsive epithelial subpopulation (E3-IFI6)
- E3-IFI6 tumor cells show spatial proximity and interaction with a myeloid subtype
- IFI6 overexpression promotes a proinflammatory activation state in macrophages

Authors

Jianli Ma, Xin Li, Niansong Qian, ..., Haitao Luo, Mingzhu Yin, Minghui Zhang

Correspondence

luoht1985@gmail.com (H.L.), yinmingzhu2008@126.com (M.Y.), zhmhuidoc@163.com (M.Z.)

In brief

Ma et al. delineate single-cell spatial atlases of LUAD tumors with rare actionable oncogenes, revealing that an IFI6-high epithelial subpopulation drives favorable immunotherapy responses. Mechanistically, IFI6 overexpression promotes proinflammatory macrophage polarization via APP-CD74 crosstalk, laying a theoretical basis for ICI therapy in rare-mutation LUAD.

Ma et al., 2026, Cell Reports Medicine 7, 102760
May 19, 2026
https://doi.org/10.1016/j.xcrm.2026.102760

CellPress

Cell Reports Medicine

CellPress
OPEN ACCESS

Article

Single-cell spatial analysis stratifies lung adenocarcinoma with rare actionable mutations and reveals immune-modulatory cellular crosstalk

Jianli Ma,[1,7] Xin Li,[2,7] Niansong Qian,[3,7] Shujin Li,[4,7] Lijun Li,[5] Xiaoxin Zhang,[5] Liqian Su,[6] Yue Yang,[6] Haitao Luo,[4,*] Mingzhu Yin,[2,*] and Minghui Zhang[2,5,8,*]

[1]Department of Radiation Oncology, Harbin Medical University Cancer Hospital, Harbin, China
[2]Clinical Research Center (CRC), Medical Pathology Center (MPC), Cancer Early Detection and Treatment Center (CEDTC) and Translational Medicine Research Center (TMRC), Chongqing University Three Gorges Hospital, Chongqing University, Chongqing, China
[3]Department of Oncology, College of Pulmonary and Critical Care Medicine, the Eighth Medical Center of PLA General Hospital, Beijing, China
[4]Kindstar Global Precision Medicine Institute, Shenzhen, China
[5]Department of Medical Oncology, Harbin Medical University Cancer Hospital, Harbin, China
[6]Department of Pathology, Harbin Medical University Cancer Hospital, Harbin, China
[7]These authors contributed equally
[8]Lead contact
*Correspondence: luoht1985@gmail.com (H.L.), yinmingzhu2008@126.com (M.Y.), zhmhuidoc@163.com (M.Z.)
https://doi.org/10.1016/j.xcrm.2026.102760

SUMMARY

Lung adenocarcinoma (LUAD) harboring distinct actionable oncogenic mutations exhibits differential responses to immune checkpoint inhibitors (ICI); however, the underlying mechanisms remain elusive. Here, we report comprehensive single-cell spatial atlases of tumors from 38 LUAD patients, predominantly harboring rare actionable oncogenes. Stratifying patients by consensus meta-programs (MP) reveals ICI-MP-H (high) and ICI-MP-L (low) subgroups. The ICI-MP-H group exhibits significant enrichment of the E3-IFI6 epithelial subpopulation, which displays high expression of interferon- and antigen presentation-related genes. Spatially, E3-IFI6 is adjacent to the Ma-MHC myeloid subpopulation; both co-enrich in a specific niche and likely interact via the APP-CD74 axis. Functional assays confirm that IFI6 overexpression in LUAD cell lines promotes proinflammatory macrophage activation. Our study systematically characterizes the features of the tumor ecosystem for different driver oncogene mutations, providing a theoretical basis for future clinical implementation of ICI therapy in patients with LUAD carrying rare mutations.

INTRODUCTION

Lung cancer remains the leading cause of cancer-related mortality worldwide, with non-small cell lung cancer (NSCLC) accounting for approximately 85% of all cases.[1] Among the subtypes of NSCLC, lung adenocarcinoma (LUAD) is the most prevalent. More than half of the patients with LUAD are diagnosed at advanced stages, when treatment is challenging and prognosis is poor. In recent years, immune checkpoint inhibitors (ICI) have revolutionized advanced-stage management; nevertheless, their benefits remain highly variable.[2] Increasing evidence from genomic studies indicates that specific actionable oncogenes promote the formation of a tumor microenvironment (TME) that influences the efficacy of ICI.[3] For instance, *EGFR* mutations typically generate an immune-suppressive TME, characterized by low tumor mutation burden, reduced infiltration by key immune cells, and attenuated immune checkpoint interactions, leading to poor responses to PD-1/PD-L1 blockade.[4–6] In contrast, *KRAS*/*TP53* co-mutant LUADs often display elevated PD-L1 expression and increased infiltration of $CD8^+$ T cells.[7,8] Nevertheless, compared to patients with *EGFR* or *KRAS* mutations, the extent to which patients with LUAD harboring rare driver mutations (conventionally defined as having a frequency of <5% in NSCLCs[9]; e.g., *RET* fusions or *MET* exon 14 skipping) can benefit from immunotherapy remains poorly understood. This critical gap in knowledge is primarily due to the limited number of clinical studies investigating immunotherapy in patients with rare driver mutations, as well as the ongoing controversies surrounding the outcomes reported in the limited literature available.[3] In this context, whether to administer ICI in clinical practice for patients carrying specific rare oncogenic driver mutations remains an urgent question to be addressed. Therefore, systematic investigations into tumor ecosystems driven by distinct oncogenic driver mutations to identify key features associated with ICI therapeutic responses hold significant value for guiding subsequent clinical research.

The advent of single-cell and spatial transcriptomics has revolutionized the study of the TME, enabling detailed analysis of

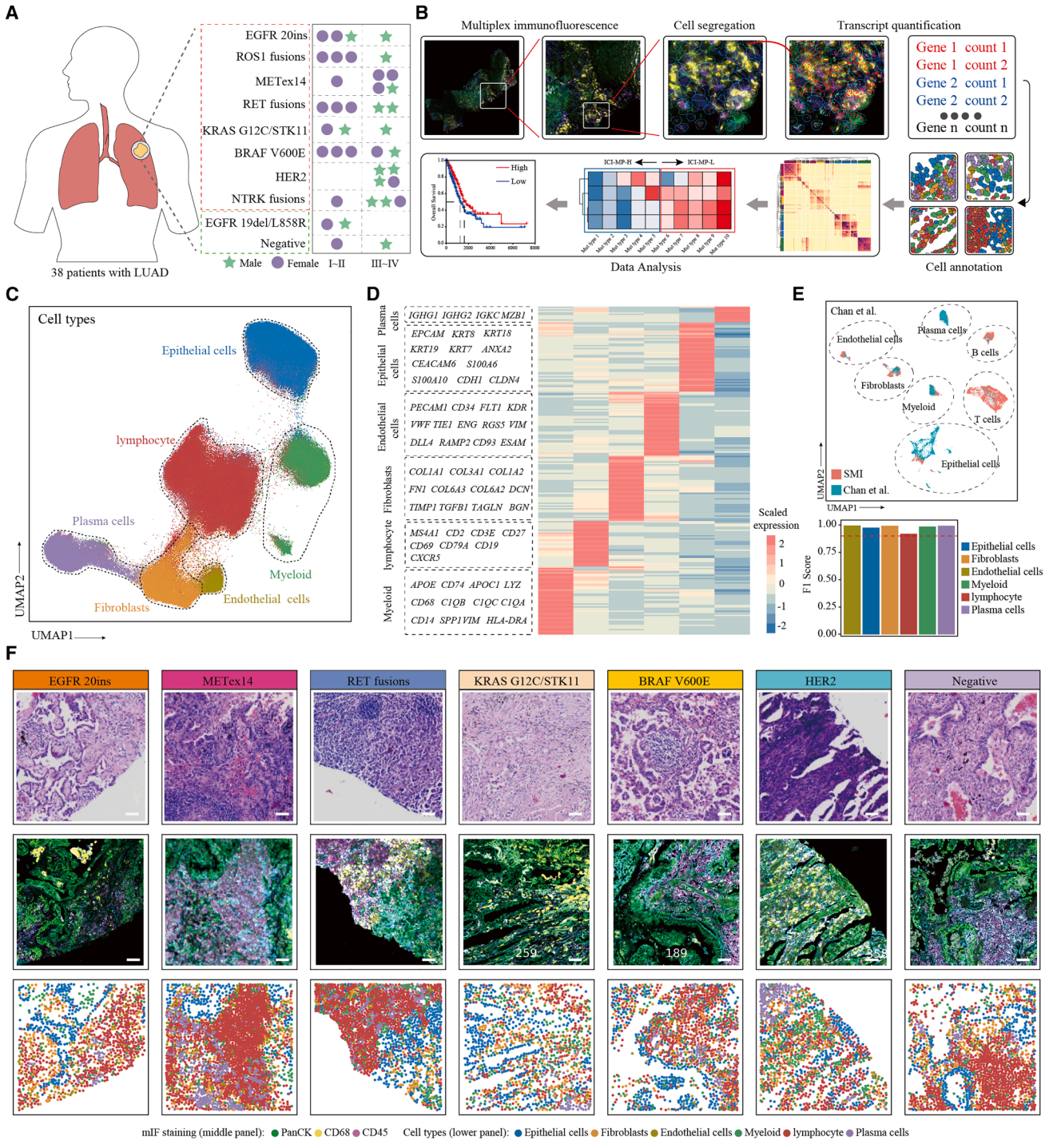

Figure 1. Single-cell spatial transcriptomic atlas of LUAD

(A) Cohort overview. Mutations highlighted in the red dashed box represent rare actionable oncogenic mutations, whereas those in the green dashed box indicate control mutation types. Each circular or star-shaped symbol corresponds to an individual sample.

(B) Study workflow.

(C) Uniform manifold approximation and projection (UMAP) plots of all cells colored based on major cell types.

(legend continued on next page)

cellular heterogeneity and interactions,[10,11] which are crucial for understanding both immunotherapy response and resistance.[12] For instance, single-cell RNA sequencing (scRNA-seq) revealed that CXCL13^{+} tumor-reactive CD8^{+} T cells are positively correlated with favorable responses to immune checkpoint blockade.[13] Additionally, studies on breast cancer have shown that the frequency of immune-regulatory dendritic cells and specific macrophage phenotypes correlates with T cell expansion following anti-PD-1 treatment.[14] Moreover, spatially resolved single-cell analyses of colorectal cancer have uncovered coordinated cellular programs that are associated with response to PD-1 blockade, with less-exhausted blood-associated tumor-reactive-like cells correlating with better treatment outcomes.[15] In NSCLC, single-cell analysis identified five distinct subtypes, with specific immune cell populations, such as natural killer cells and memory B cells, linked to major pathological response (MPR), whereas higher levels of CCR8+ regulatory T cells (Tregs) were found in non-MPR (NMPR) patients, offering valuable insights for personalized treatment strategies.[16] Therefore, leveraging single-cell spatial transcriptomics to investigate the TME in patients with LUAD harboring rare driver mutations is essential for uncovering actionable insights into the treatment response and optimizing patient stratification in clinical practice.

In this study, to comprehensively characterize the TME features of LUAD driven by different rare actionable oncogenes, we collected tumor samples from 38 patients with LUAD carrying different types of oncogenic mutations. Based on single-cell spatial molecular imaging (SMI) technology, we systematically characterized the heterogeneity of the TME across all mutation types and identified molecular features associated with ICI responses. Based on these features, we stratified the patients and investigated the TME differences across the stratified subgroups.

RESULTS

Single-cell spatial atlases of LUAD harboring distinct actionable oncogene mutations

To comprehensively characterize the TME features of LUAD driven by different rare oncogenic mutations, we prospectively collected paraffin-embedded tissue samples from 38 patients with LUAD (Figure 1A; Table S1). They included 34 patients with eight types of rare actionable oncogenic mutations, namely, EGFR exon 20 insertions (EGFR 20ins, 4 cases), ROS1 fusions (4 cases), MET exon 14 skipping mutations (METex14, 5 cases), RET fusions (5 cases), KRAS G12C/STK11 co-mutations (3 cases), BRAF V600E mutations (5 cases), HER2 mutations (4 cases), and NTRK fusions (4 cases). The remaining 4 samples served as reference groups, which have well-studied associations with immunotherapy outcomes, consisting of 2 cases with EGFR exon 19 deletions/L858R mutations (EGFR 19del/L858R, common EGFR mutations) and 2 cases without identifiable actionable oncogenes (negative cases). All samples were analyzed using the NanoString CosMx SMI platform, which provides both single-cell transcriptomic and spatial information (Figure 1B). After rigorous quality control and filtering, 486,163 cells were retained from the 38 samples (Figure S1A; Table S2). By integrating both the intrinsic gene expression of individual cells and the expression levels of their neighboring cells, we utilized a spatially informed clustering approach to identify the major cell types.[17] The cell types were annotated based on the expression of classical marker genes, including epithelial cells (23.65%), lymphocytes (36.8%), plasma cells (10.51%), myeloid cells (12.46%), fibroblasts (12.72%), and endothelial cells (3.86%) (Figures 1C, 1D, S1B, and S1C). To further confirm the accuracy of the main cell-type annotations, we employed two additional methods. First, we compared the SMI data with a publicly available scRNA-seq dataset.[18,19] Cell-type annotations based on SMI were highly consistent with those from the reference datasets, with an average F1 score exceeding 0.9 across all major cell types (Figure 1E). Second, we validated the annotations against multiplex immunofluorescence (mIF) and hematoxylin and eosin (H&E) staining of matched tissue sections. For each sample, pathologists examined the concordance between annotated cell types and the histopathological features (Figure 1F). The results validated the accuracy and reliability of the SMI-based cell-type annotations.

Stratification of patients with LUAD based on molecular features associated with ICI responses

To capture the differences between the samples driven by different rare actionable oncogenes, we first calculated the proportions of the major cell types across all samples and performed principal-component analysis based on the cell composition. Results showed that cell composition was relatively uniform across different samples (Figures 2A and 2B), indicating that LUAD driven by different oncogenic mutations did not exhibit significant differences in the overall cellular composition. Given the lack of remarkable differences in cell composition, we applied consensus non-negative matrix factorization (cNMF) to identify gene expression programs and uncover heterogeneity associated with different oncogenic mutations. The cNMF analysis identified 13 consensus meta-programs (MPs), which were shared across all samples (Figures 2C; Table S3). We compared the MPs with the well-established recurrent MPs conserved across diverse tumor types, as defined by the Curated Cancer Cell Atlas (3CA).[18] Notable concordance was detected between the two MP collections, indicating the robustness and validity of our identified MPs (Figure 2D). Based on the marker genes enriched in each MP and the results of the 3CA comparison, the identified MPs could be primarily categorized into three major classes, namely, tumor cell-associated MPs (MP5/6/10), immune-associated MPs (MP2/4/7/8/9/16/17), and stroma-associated MPs (MP3/13/14) (Figure 2D).

(D) Heatmap depicting the expression of selected marker genes, across major cell types in LUAD. Rows represent genes, and columns represent cell types. *p* values were adjusted for multiple testing using the Benjamini-Hochberg method.

(E) Validation of SMI data accuracy by co-embedding with published scRNA-seq data (upper); F1 score of the co-embedding results (lower).

(F) *In situ* spatial maps of different mutation types. Hematoxylin and eosin (H&E) images (upper, scale bars, 10 μm, n = 7 biological replicas), SMI multicolor immunofluorescence images (middle, scale bars, 10 μm, n = 7 biological replicas), and annotated cell types (lower).

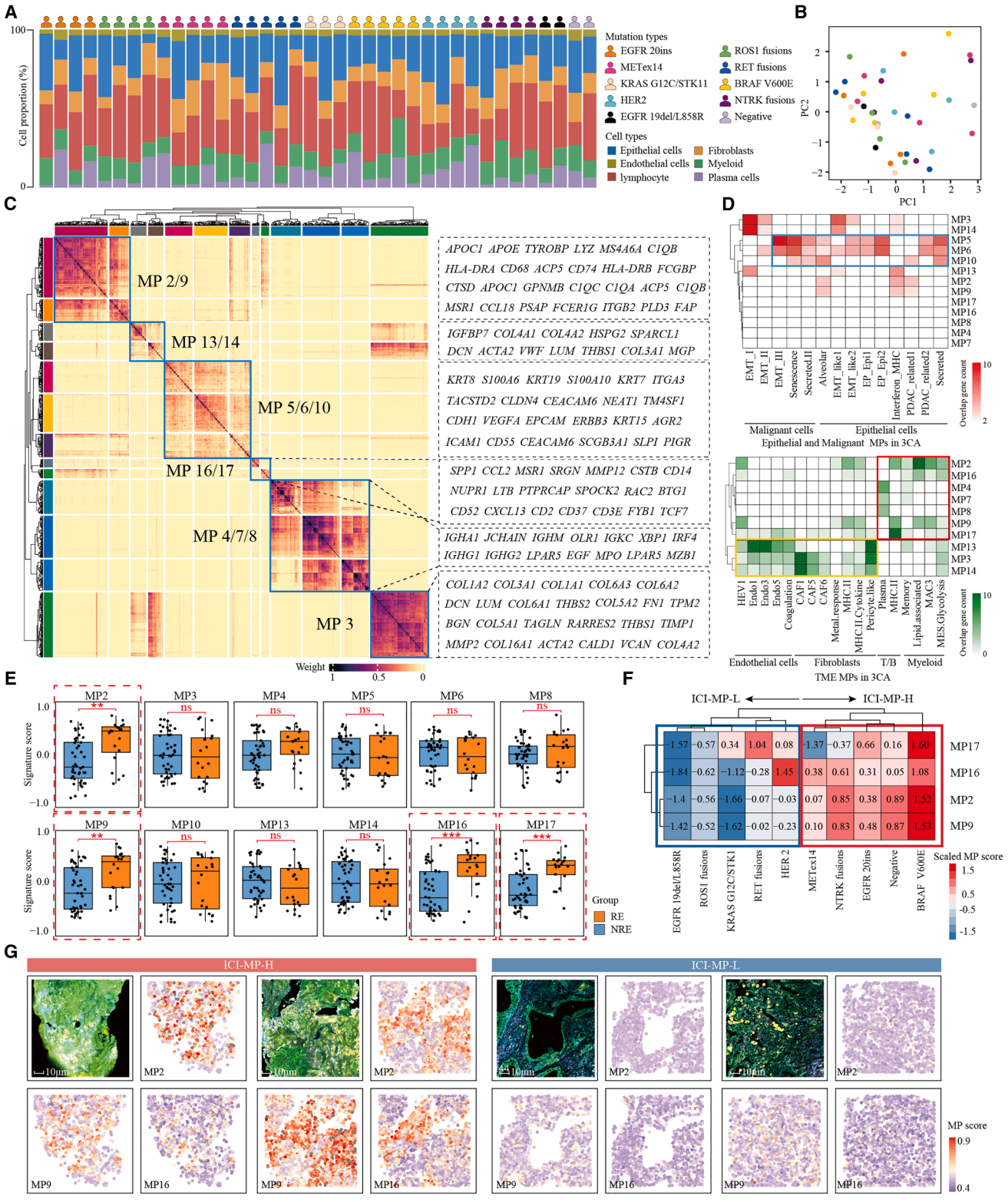

Figure 2. MP analysis and stratification of LUAD patients based on molecular features associated with ICI responses

(A) Bar plots showing the proportions of six major cell types in LUAD samples.

(B) Principal-component analysis based on the cell proportion of each sample. Each point represents a sample, with colors indicating oncogenic mutation types.

(C) Heatmap of MPs identified by consensus non-negative matrix factorization analysis. The marker genes of each MP are listed on the right side.

(legend continued on next page)

Next, we aimed to identify which MPs are associated with ICI therapeutic responses. To this end, we collected three bulk RNA sequencing (RNA-seq) datasets from LUAD cohorts with well-documented ICI treatment outcomes and assessed the expression level of each MP in individual samples. Comparing the MPs that displayed significant differences between ICI responders and non-responders, we identified four ICI response-associated MPs (MP 2/9/16/17), all showing a high expression pattern in the ICI responder group (Figure 2E). Furthermore, we generated a combined signature through comprehensive characterization of the four MPs. In The Cancer Genome Atlas (TCGA) LUAD cohort, patients with high expression of this signature exhibited significantly better prognosis ($p = 0.0048$) (Figure S2A). Based on the expression patterns of the four ICI response-associated MPs across samples with different oncogenic mutations, we stratified eight rare mutation types together with two reference categories (EGFR 19del/L858R mutations and negative cases) into two distinct subgroups, namely, the ICI response-associated MPs high-expression group (ICI-MP-H) and the ICI response-associated MPs low-expression group (ICI-MP-L) (Figure 2F). The expression patterns were additionally observed in the spatial context (Figures 2G and S2B). Specifically, samples with ROS1 fusions, RET fusions, KRAS G12C/STK11, HER2 mutations, or EGFR 19del/L858R were assigned to the ICI-MP-L group, while those with EGFR 20ins, METex14, BRAF V600E, NTRK fusions, or negative cases were categorized into the ICI-MP-H group (Figure 2F). Existing evidence demonstrates that LUAD patients with EGFR 19del/L858R mutations respond poorly to ICI therapy, whereas those with actionable oncogene-negative status could derive clinical benefit from ICI treatment.[3] Nevertheless, the efficacy of ICI therapy in patients harboring rare actionable oncogenic mutations remains controversial. To address this, we performed a comprehensive literature search to systematically and unbiasedly curate relevant clinical studies and analyzed ICI treatment outcomes across patients with distinct rare actionable oncogenic mutations. Our findings revealed that patients with mutation types belonging to the ICI-MP-H group (e.g., BRAF and METex14 mutations) displayed favorable objective response rates and progression-free survival, whereas patients in the ICI-MP-L group (e.g., RET fusions and HER2 mutations) demonstrated poor prognosis following immunotherapy (Figure S2C). These observations thus support the validity of our proposed stratification results.

The epithelial cell subpopulation associated with the interferon response process is enriched in the ICI-MP-H group

Building on the aforementioned stratification of oncogenic mutations, we first examined the differential gene expression profiles in tumor epithelial cells between the two groups. The results revealed that, compared with the ICI-MP-L group, the tumor epithelial cells in the ICI-MP-H group exhibited significantly elevated expression levels of genes related to human leukocyte antigen and interferon response processes (Figure S3A; Table S4). Gene enrichment analysis further highlighted the significant enhancement of these pathways in the ICI-MP-H group (Figure S3B), suggesting that the major histocompatibility complex (MHC) and interferon secretion process in tumor cells of this group is more active.

To explore the potential mechanisms underlying the differences in tumor heterogeneity, we performed a re-clustering analysis of the epithelial cells and classified them into 6 subpopulations (Figures 3A and 3B). Based on the most specific genes for each subpopulation, we named each epithelial cell subpopulation as E0-POU5F1, E1-ANXA2, E2-SAT1, E3-IFI6, E4-COL1A1, and E5-SERPINA1 (Figures 3A and 3B; Table S5). Among them, the E3-IFI6 cluster was found to be significantly more abundant in the ICI-MP-H group than in the ICI-MP-L group (Figure 3C), a phenomenon that was particularly evident in the spatial distribution of the cells (Figure 3D), further confirming the enrichment of E3-IFI6 cells in the ICI-MP-H group. As expected, using the "AddModuleScore" algorithm, we detected specific enrichment of genes involved in the interferon response process in E3-IFI6 (Figure 3E). Within the spatial context, high-magnification image analysis confirmed the expression of E3-IFI6 marker genes (e.g., *IFI6* and *IFITM1*) in these cells (Figure 3F). We then conducted mIF experiments for further validation. Quantitative results at the protein level revealed that the number of cells positive for E3-IFI6 key marker genes (e.g., PanCK and IFI6) was significantly higher in the ICI-MP-H group than in the ICI-MP-L group (Figure 3G). To test the robustness of E3-IFI6-related molecular features across samples, we performed cNMF analysis on tumor epithelial cells and identified 5 epithelial MPs (E-MPs) (Figure 3H). We next assessed the expression levels of E-MPs in the E3-IFI6 subset and found that E-MP3 showed the highest expression within this subset (Figure 3I). Concomitantly, the E-MP3 score was significantly elevated in the ICI-MP-H group than in the ICI-MP-L group (Figure 3J). To examine whether E3-IFI6 is associated with clinical ICI therapy, we analyzed a set of LUAD scRNA-seq data that included explicit immune therapy response information (Figure S3C).[20] Results showed that the expression of E3-IFI6 marker genes in the epithelial cell population of the MPR group was significantly higher than that in the epithelial cell populations of both the NMPR group and the treatment naive (TN) group, implying a potential association between E3-IFI6 and immune therapy response (Figure 3K).

(D) Comparison results between the MPs we identified and those in the Curated Cancer Cell Atlas (3CA) database. (Upper) The comparison with MPs derived from epithelial/malignant cells in the 3CA database, and (lower) the comparison with MPs of TME origin in the 3CA database.

(E) Boxplots illustrate the comparative differences in different MPs between the responder (RE, $n = 20$) group and non-responder (NRE, $n = 45$) group among NSCLC patients receiving immunotherapy. Each dot represents an individual sample.

(F) Heatmap showing the standardized MP scores of MP2, MP9, MP16, and MP17 signatures across different oncogenic mutation types. The mutation groups were determined by unsupervised hierarchical clustering using Canberra distance and the Ward.D method.

(G) The mIF images and corresponding spatial *in situ* maps demonstrate the ICI response-associated MP signature scores between the two groups. Scale bars, 10 μm. $n = 4$ biological replicas. mIF staining: PanCK(green), CD68 (yellow), CD45 (pink).

Statistical analysis was performed using the Wilcoxon test. $^{**}p < 0.01$, $^{***}p < 0.001$; ns, no significant difference.

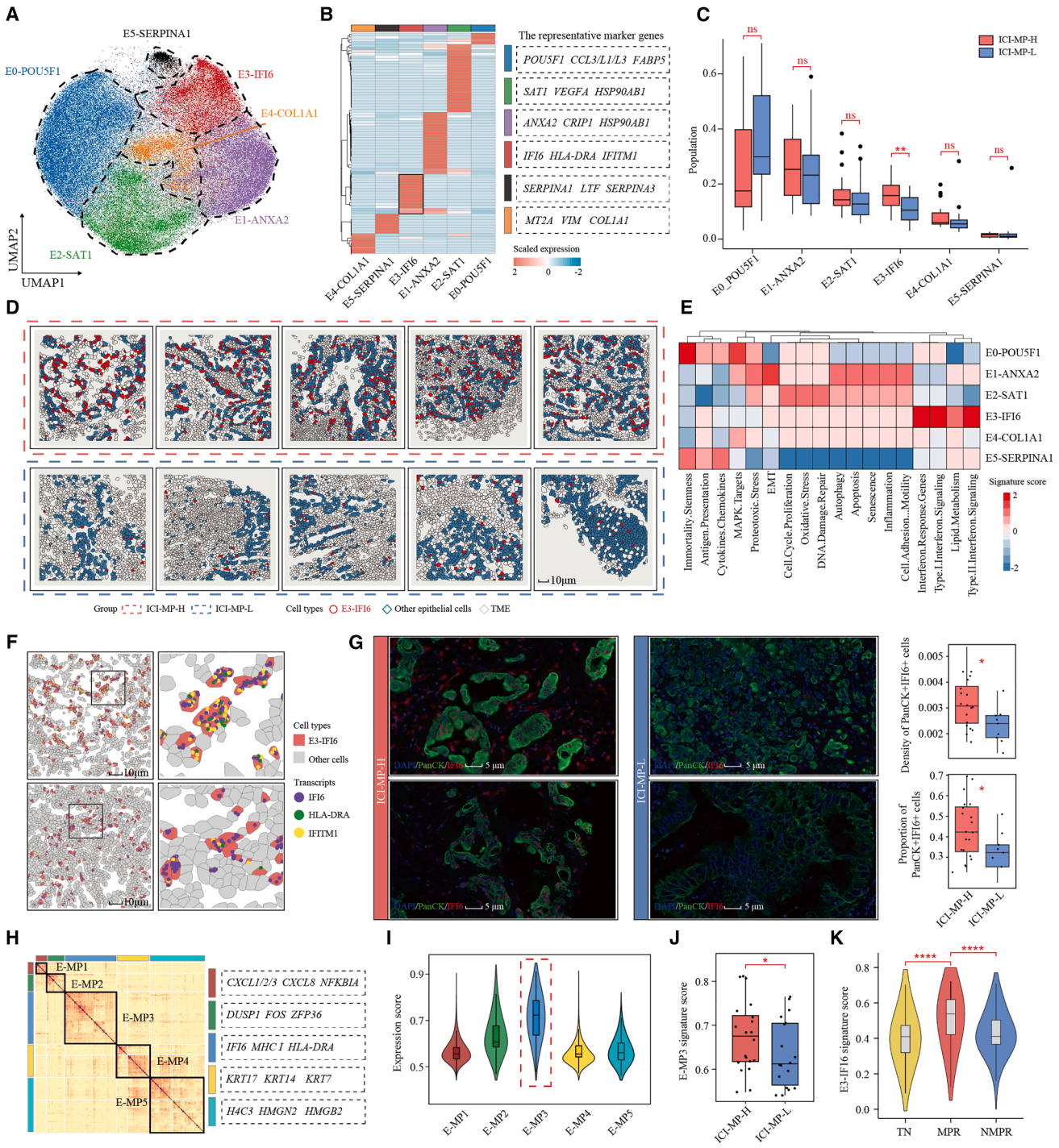

Figure 3. The identification of epithelial cell subpopulations and their molecular characteristics in the ICI-MP-H and ICI-MP-L groups

(A) UMAP plot of epithelial subpopulations.

(B) Heatmap showing the expression of marker genes of epithelial cell subpopulations. The representative marker genes for each epithelial cell subset are displayed on the right side. *p* values were adjusted for multiple testing using the Benjamini-Hochberg method.

(C) Boxplot showing the proportion of epithelial cell subpopulations in the ICI-MP-H and ICI-MP-L groups (ICI-MP-H, *n* = 20; ICI-MP-L, *n* = 18). Each dot represents an individual sample.

(D) Representative samples of spatial *in situ* maps for the ICI-MP-H and ICI-MP-L groups. Scale bar, 10 μm.

(E) Heatmap illustrates the results of biological pathway activity analysis across various epithelial cell subtypes based on the "AddModuleScore" algorithm.

(legend continued on next page)

E3-IFI6 exhibits spatial proximity with a myeloid subtype and sustains anti-tumor immune activity in macrophages

To investigate the spatial relationship between E3-IFI6 cells and the major cell types in the TME, we conducted a spatial distribution analysis. We first calculated the spatial co-occurrence scores between E3-IFI6 cells and various cell types in the TME and found the E3-IFI6 cells to be closest to myeloid cells (Figures 4A and S4A). Furthermore, for each sample, we assessed the occurrence probability of different TME cell types within distinct spatial distances from E3-IFI6 cells and confirmed that myeloid cells tend to cluster around E3-IFI6 cells (Figure 4B). Through spatial visualization, we directly demonstrated the spatial distribution of E3-IFI6 cells and myeloid cells, confirming their proximity in the tissue (Figure 4C). When comparing the major cell composition between the ICI-MP-H and the ICI-MP-L groups, we observed the proportion of myeloid cells in the ICI-MP-H group to be significantly higher than that in the ICI-MP-L group (Figure 4D).

To further explore the heterogeneity of myeloid cells and identify the myeloid subpopulation that is most strongly associated with E3-IFI6, we categorized myeloid cells into 3 major classes, including macrophages (Ma), dendritic cells (DC), and monocytes (Mo), and 9 subpopulations, namely, Ma-TIMP1, Ma-MMP9, Ma-MHC, Ma-SPP1, pDC-PLAC8, pDC-CCR7, Mo-CD16^{+}, Mo-intermediary, and Mo-CD14^{+} cells (Figure 4E). The marker genes of each myeloid subpopulation exhibited high specificity (Figure S4B). By comparing the correlations between E3-IFI6 and various myeloid subpopulations across all samples, we found E3-IFI6 to have the strongest correlation with Ma-MHC (Figure 4F). Meanwhile, among all the myeloid subpopulations, Ma-MHC exhibited the strongest spatial colocalization and cell-cell interaction signals with E3-IFI6 (Figures 4G and S4C and 4D), and their colocalization could be visually observed in the spatial context (Figure S4E). Additionally, we examined the proportion distribution of various myeloid subtypes across samples with different mutation types and compared the distribution differences between the ICI-MP-H and ICI-MP-L groups (Figure S4F). Results showed that the proportion of Ma-MHC was significantly higher in the ICI-MP-H group than in the ICI-MP-L group (Figure 4H). Concurrently, among all myeloid subtypes, the antigen presentation signature score exhibited the strongest activity in Ma-MHC cells (Figure S4G). At the protein level, we employed mIF assays to validate that the macrophage subset (CD68+HLA-DRB+ cells), which expresses Ma-MHC cell marker genes and exhibits antigen presentation function, was highly enriched in the ICI-MP-H group (Figure 4I). Collectively, the findings indicated that the spatial proximity between E3-IFI6 and Ma-MHC, together with their potential interactions, might enhance immune activity in the ICI-MP-H group.

Subsequently, we conducted experiments to validate the effect of tumor cells with high *IFI6* expression on the immune activity of macrophages, aiming to elucidate the underlying mechanism by which the interaction between E3-IFI6 and Ma-MHC mediates favorable responses to immunotherapy. Following the screening of genetic mutation profiles across various NSCLC cell lines, we selected two LUAD cell lines, NCI-H1975 and NCI-H23, which harbor mutations belonging to the ICI-MP-L group. After the successful establishment of *IFI6*-overexpressing cell lines (Figures 4J and 4K), we performed Transwell co-culture assays of these tumor cell lines with M0 macrophages (Figure 4L). The results demonstrated that co-culture of *IFI6*-overexpressing tumor cells with macrophages markedly upregulated the expression of proinflammatory genes, including *HLA-DRB*, *IL-12*, *CD86*, and *TNF-*α, whereas the expression levels of anti-inflammatory genes such as *CD163*, *CD206,* *TGF-*β, and *ARG1* were significantly downregulated under the same conditions (Figures 4M and S4H). These findings suggest that tumor cells with high *IFI6* expression can sustain the anti-tumor immune activity of macrophages, which may represent the potential mechanism underlying the superior immunotherapeutic efficacy observed in the ICI-MP-H group.

E3-IFI6 and Ma-MHC cells are enriched in a specific spatial niche within the ICI-MP-H group and interact with each other

To further explore whether the interaction between E3-IFI6 and Ma-MHC cells occurs in a specific region within tumor tissues, we conducted an in-depth analysis of spatial niches across all tumor tissues. Using a spatially informed niche identification strategy, we identified 13 distinct niches, including one niche dominated by epithelial and myeloid cells (EMD), three lymphocyte-dominated niches (LD), two stromal cell-dominated niches (SD), and four niches with mixed cell types (MD) (Figures 5A and 5B). Comparing the distribution of different cell types in each niche between the ICI-MP-H and ICI-MP-L groups, we found the number of E3-IFI6 and Ma-MHC cells to be significantly higher in Niche0 in the ICI-MP-H group (Figures 5C and S5A). Concurrently, we observed that E3-IFI6 and Ma-MHC cells were primarily enriched in Niche0 specifically, with 58.2% of E3-IFI6 cells and 43.4% of Ma-MHC cells localized within Niche0 (Figures 5D and 5E). Evaluation of spatial distances between

(F) Spatial *in situ* maps show the *in situ* visualization of the E3-IFI6 subset and its corresponding marker gene transcripts (scale bars, 10 μm, n = 2 biological replicas).
(G) The multicolor immunofluorescence images demonstrate that the E3-IFI6 cells (PanCK+ and IFI6+) are present in significantly higher numbers in the ICI-MP-H group samples compared to the ICI-MP-L group samples (Scale bars, 5 μm, n = 4 biological replicas). Boxplots showing the statistical results of differences between the two groups are displayed on the right side, n (ICI-MP-H) = 20, n (ICI-MP-L) = 9.
(H) Heatmap showing the MPs of epithelial cells. The representative marker gene of each MP is displayed on the right side.
(I) Violin plots show the expression levels of different epithelial meta-programs (E-MPs) in the E3-IFI6 cells.
(J) Boxplot showing the E-MP3 signature score in ICI-MP-H and ICI-MP-L groups (ICI-MP-H, n = 20; ICI-MP-L, n = 18). Each dot represents an individual sample.
(K) Violin plot showing the E3-IFI6 signature score in epithelial cell populations of treatment-naive (TN), major pathologic response (MPR), and non-major pathologic response (NMPR) groups. Statistical analysis was performed using a two-tailed unpaired t test. *p < 0.05, **p < 0.01, ****p < 0.0001; ns, no significant difference.

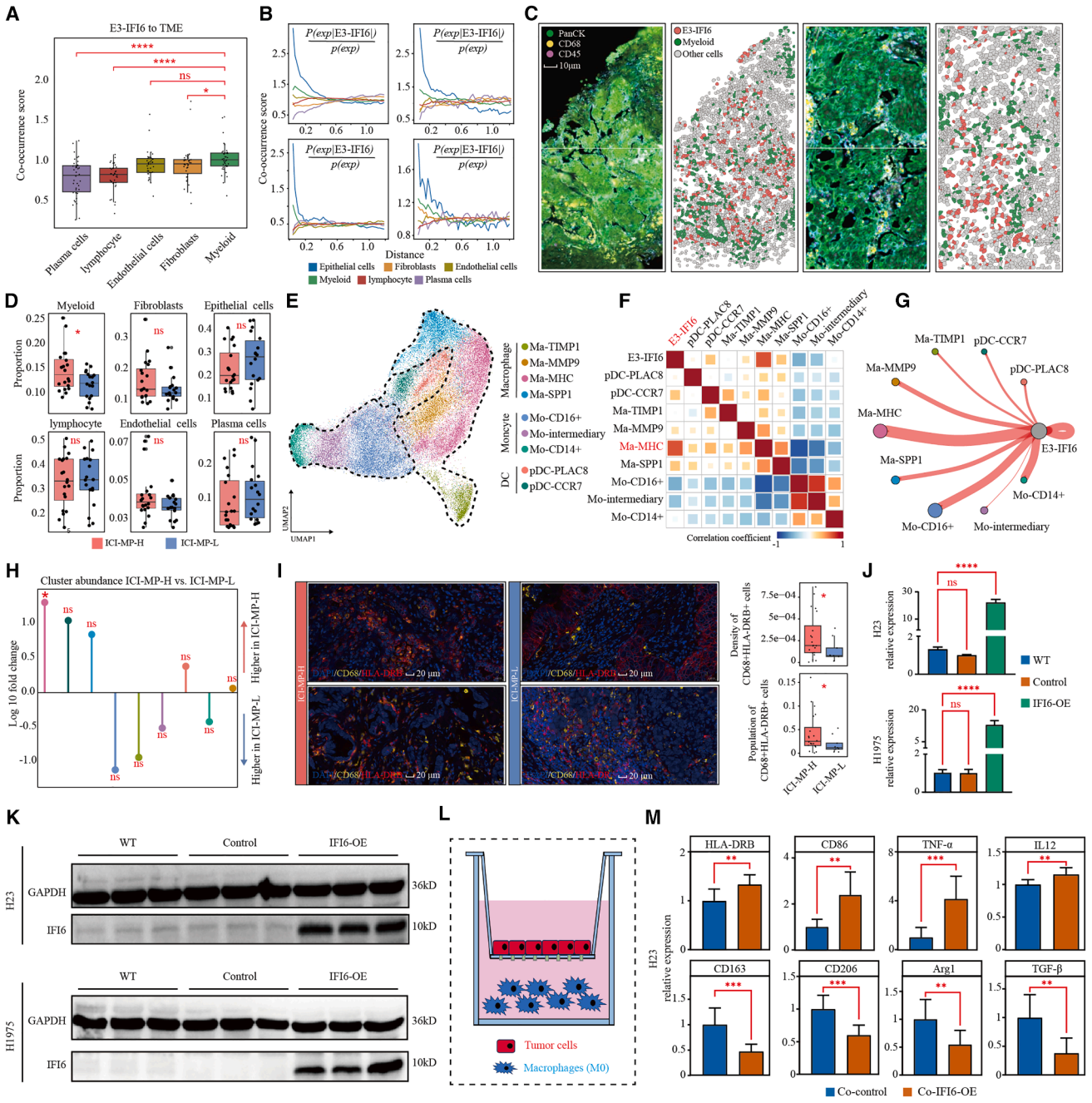

Figure 4. Spatial characteristics and potential biological mechanisms between E3-IFI6 and Ma-MHC subsets

(A) Boxplot showing the co-occurrence score between E3-IFI6 and major cell types in the TME. Each dot represents an individual sample, *n* = 38.

(B) Co-occurrence probability of E3-IFI6 with other TME cells at different distance ranges.

(C) mIF images and corresponding spatial *in situ* maps demonstrate that E3-IFI6 exhibits spatial proximity to myeloid cells (scale bar: 10 μm, *n* = 2 biological replicas).

(D) Boxplots showing the proportion of major cell types in the ICI-MP-H and ICI-MP-L groups (ICI-MP-H, *n* = 20; ICI-MP-L, *n* = 18). Each dot represents an individual sample.

(E) UMAP plot of myeloid cells, colored for 9 subpopulations.

(F) Heatmap displaying the correlation between the proportions of E3-IFI6 and myeloid cell subpopulations across all samples.

(G) Circos plot displaying the putative ligand-receptor interactions between E3-IFI6 and myeloid cell subpopulations.

(H) Comparison of the proportion of myeloid cell subpopulations in ICI-MP-H and ICI-MP-L groups (ICI-MP-H, *n* = 20; ICI-MP-L, *n* = 18).

(legend continued on next page)

Niche0 and others revealed that Niche0 was in closest proximity to Niche9, which consists of multiple cell types in comparable proportions (Figure 5F). Analysis of genes specifically expressed in Niche0 indicated that this region primarily exhibits activation of pathways such as immune response and inflammatory response (Figure S5B).

Given the strong interaction between E3-IFI6 and myeloid cells, we conducted a cell-cell interaction analysis of E3-IFI6 with all myeloid subpopulations. Comparing the most significant ligand-receptor pairs between the ICI-MP-H and ICI-MP-L groups, we identified 17 pairs, with 12 significantly enriched in the ICI-MP-H group and 5 in the ICI-MP-L group (Figure 5G). Subsequently, we focused on the interaction between E3-IFI6 and Ma-MHC and found E3-IFI6 cells to mainly express ligands related to the mIF, APP, and VEGFA families, while the APP-CD74 axis ranks first among receptor signals in Ma-MHC cells (Figure 5H). Furthermore, the interaction signal between E3-IFI6 and Ma-MHC via the APP-CD74 axis was more pronounced in the ICI-MP-H group (Figure 5I).

To validate the above biological knowledge-driven analyses based on cell subsets and ligand receptors, we employed the data-driven, unbiased InSituCor algorithm,[21] which identifies co-expressed gene modules in specific spatial regions by screening genes with spatial correlation, independent of cell-type distribution. Results demonstrated that *APP* and *CD74* are co-expressed in the antigen-linked interaction module, which shows spatial overlap with Niche0 (Figure 5J). The module is closely associated with immune inflammation and extracellular matrix remodeling modules (Figure 5K). We further utilized mIF to visualize APP and CD74 proteins and directly observed the crosstalk between IFI6+ tumor cells and HLA-DRB+ macrophages (Figure 5L). Additionally, in LUAD RNA-seq data with ICI outcomes, both E3-IFI6 and Ma-MHC signature scores were significantly higher in responders than non-responders ($p < 0.05$), further suggesting their association with favorable ICI response (Figures S5C and S5D). We then constructed a Cox regression model based on the E3-IFI6 signature, Ma-MHC signature, and the combined signature to analyze their impacts on patient prognosis (Figure 5M). Results showed that the combined signature was significantly associated with better prognosis, with higher combined signature score correlating with longer overall survival in patients (Figure 5N). Collectively, our findings suggested that E3-IFI6 and Ma-MHC are specifically enriched in a distinct spatial niche and may interact via the APP/CD74 axis, with their signature holding potential predictive value for immunotherapeutic response and clinical prognosis.

DISCUSSION

Molecular subtyping of LUAD based on driver gene mutations has become a critical foundation for current clinical treatment decisions.[22,23] For patients with LUAD bearing common mutations, a preliminary consensus has been reached regarding their response to ICI; for instance, patients with KRAS G12C mutations often respond well to ICI therapy,[22] whereas those with EGFR-sensitive mutations tend to show poor response.[4,6] However, for patients harboring rare driver mutations, such as ROS1, MET, and RET, a systematic understanding of their response to immunotherapy remains limited due to the scarcity of tumor tissue samples.[10,23,24] In this study, we analyzed LUAD samples with various rare driver mutations using CosMx SMI technology to systematically characterize their tumor ecosystems. We identified key molecular features associated with ICI treatment efficacy and stratified LUADs harboring rare actionable oncogenes into two subgroups based on these ICI response-related signatures. We then systematically analyzed the TME characteristics of LUAD in different groups at single-cell spatial resolution and identified an epithelial cell subpopulation enriched in the ICI-MP-H group, which exhibits spatial proximity to and interaction with a myeloid subtype. Our study provides a theoretical basis and valuable reference for future clinical studies on immunotherapy targeting LUADs harboring rare actionable oncogenes.

Our study revealed that LUAD samples with EGFR 20ins, BRAF V600E, METex14, and NTRK mutations exhibited typical "hot tumor" characteristics, while samples with ROS1 fusions, KRAS G12C/STK11, RET fusions, and HER2 mutations displayed "cold tumor" characteristics. Specifically, in samples harboring response-associated mutations (e.g., BRAF V600E, EGFR 20ins, and METex14), the antigen presentation pathway was significantly activated, marked by the upregulation of HLA and interferon-related genes. This enhanced immunogenic profile was reflected in the enrichment of the E3-IFI6 epithelial cell subset, suggesting its critical role in regulating immune responses. Moreover, we found that E3-IFI6 cells exhibit spatial proximity and interaction with a myeloid subtype possessing antigen-presenting activity, and this interaction between the two cell subsets is potentially mediated via the APP-CD74 axis. Notably, these observations were consistent with the findings by Hu et al., who reported that, following treatment, tumor cells from patients in the MPR group exhibited high expression of CD74 and MHC-related genes.[25] Regarding the rationality of our stratification, we systematically reviewed and summarized

(I) The multicolor immunofluorescence images demonstrate that the Ma-MHC cells ($CD68^+$, HLA-DRB+) are present in significantly higher numbers in the ICI-MP-H group samples compared to the ICI-MP-L group samples (scale bars, 20 μm, $n = 4$ biological replicas). Boxplots showing the statistical results of differences between the two groups are displayed on the right side, n (ICI-MP-H) = 20, n (ICI-MP-L) = 9.

(J) Relative mRNA expression of IFI6 in wild-type (WT), vector control (control), and IFI6-overexpression (IFI6-OE) H23 and H1975 cells. $n = 3$ technical replicas.

(K) Western blot analysis of IFI6 protein expression in H23 and H1975 cells across WT, control, and IFI6-OE groups. $n = 3$ technical replicas.

(L) Schematic illustration of the Transwell co-culture system.

(M) Relative mRNA expression of representative pro-inflammatory and anti-inflammatory genes in macrophages following co-culture with control or IFI6-OE tumor cells (H23). $n = 3$ technical replicas.

Statistical comparisons between two groups were performed using a two-tailed unpaired t test. For comparisons among multiple groups, one-way ANOVA followed by Tukey's post hoc test was employed. The data are presented as the means ± SD. $^*p < 0.05$, $^{**}p < 0.01$, $^{***}p < 0.001$, $^{****}p < 0.0001$; ns, no significant difference.

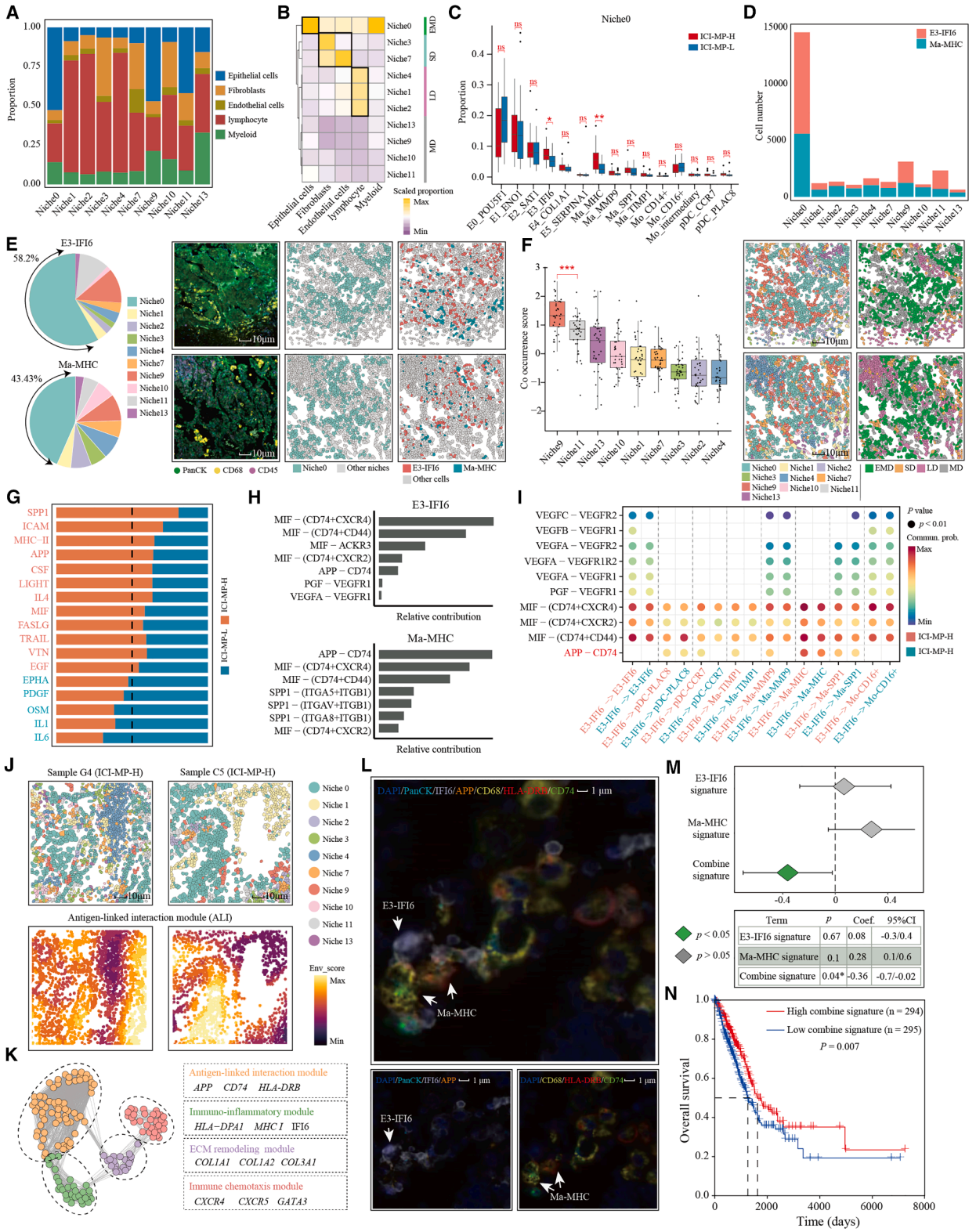

Figure 5. Spatial niche analysis and dissection of the signaling crosstalk between E3-IFI6 and Ma-MHC cells

(A) Bar plot showing the proportions of major cell types within each niche.

(B) Heatmap displaying the distribution of each cell type across niches, with niches grouped into four categories.

(legend continued on next page)

international clinical studies on immunotherapy for LUAD with rare mutations that have been conducted to date. The results reveal that patients with mutation types classified under the ICI-MP-H group (e.g., EGFR, BRAF, and METex14 mutations) exhibited favorable clinical prognoses. Our *in vitro* functional assays further corroborated the potential mechanistic link between IFI6 expression and macrophage polarization in LUAD: IFI6 overexpression in tumor cells was found to drive M0 macrophages toward a proinflammatory phenotype, as evidenced by the upregulated expression of proinflammatory genes and concurrent downregulation of anti-inflammatory markers upon Transwell co-culture. These observations support a potential role of IFI6 in sustaining the anti-tumor immune activity of macrophages, which may partially underpin the favorable immunotherapeutic responses associated with the E3-IFI6 and Ma-MHC-enriched ICI-MP-H subtype.

To validate the cellular interaction between E3-IFI6 and Ma-MHC, we performed mIF experiments to examine the protein expression and spatial proximity of these cells. Encouragingly, this image-based analysis allowed us to clearly observe E3-IFI6 cells expressing APP protein in close proximity to Ma-MHC cells expressing CD74. This observation provides direct spatial and protein-level evidence supporting the role of the APP-CD74 axis in E3-IFI6 and Ma-MHC cell interactions. Additionally, we found E3-IFI6 and Ma-MHC cells to possibly serve as potential biomarkers for predicting ICI response and prognosis. Their combined signatures could enable effective pretreatment stratification to identify the patients most likely to benefit from ICI. Spatial TME analysis lays the foundation for the development of combination therapies—for example, enhancing the recruitment or functional activation of Ma-MHC cells in the TME might help immunologically ''cold'' tumors to acquire immunogenic ''hot'' phenotypes, increasing their sensitivity to immunotherapy. Collectively, these findings underscore the significance of stratifying LUADs harboring rare actionable oncogenes based on ICI response-related signatures, as well as the clinical relevance of TME characteristics, thereby offering valuable insights to guide future translational and clinical research.

Limitations of the study

Several limitations of the present study should be acknowledged, along with directions for future investigation. First, LUAD patients harboring rare actionable oncogenes in our cohort did not receive immunotherapy. While we validated the rationale for patient stratification by synthesizing findings from global clinical studies, direct clinical evidence supporting this stratification remains lacking. Building on current observations, we plan to initiate clinical trials focusing on LUAD patients with mutation types exhibiting ''hot tumor'' characteristics to address this gap. Second, the heterogeneity of our study cohort stems not only from differences in patients' driver mutations but also primarily from variations in smoking history. Prior studies have shown that smoking history correlates with differential immunotherapy responses in LUAD patients.[3] This highlights the need for future studies leveraging larger, more comprehensive patient cohorts to mitigate such confounding effects. Third, the public datasets used for patient stratification and validation have inherent limitations. These arise from the heterogeneity of patient samples, disparities in prior treatment regimens, and the absence of immunotherapy cohort data across different mutation types. Additionally, the TCGA dataset and bulk RNA-seq data lack the resolution to capture the spatial relationships we identified. This further constrains the generalizability of our spatial findings. Fourth, while the CosMx platform enabled our single-cell spatial analyses, as a relatively emerging technological tool, it requires rigorous technical validation. Due to resource constraints and the focused scope of our initial experimental design, we did not perform repeated CosMx SMI analyses on the same samples at distinct time points to assess technical reproducibility. Moreover, the current CosMx SMI panel does not cover the full transcriptome, which may limit the ability to effectively distinguish and identify certain cell subsets such as conventional dendritic cells. Future single-cell spatial omics studies leveraging whole-transcriptome profiling may uncover additional biological insights. Finally, although we validated the effect of IFI6-expressing tumor cells on macrophage activity using cellular assays and observed the intercellular interaction between target cell populations via the APP-CD74 axis by mIF,

(C) Boxplot showing differences in the proportions of epithelial and myeloid cell subtypes between ICI-MP-H and ICI-MP-L groups within Niche0 (ICI-MP-H, n = 20; ICI-MP-L, n = 18). Each dot represents an individual sample.
(D) Bar plot showing the number of E3-IFI6 and Ma-MHC cells across niches.
(E) Pie charts showing the distribution of E3-IFI6 (top) and Ma-MHC (bottom) cells across niches (left) and their spatial localization within Niche0 (right). Scale bar, 10 μm, n = 2 biological replicas.
(F) Boxplot showing the co-occurrence score between Niche0 and other niches (left), n = 38. The spatial *in situ* map on the right shows the spatial localization between Niche0 and Niche9. Scale bars, 10 μm.
(G) Cell-cell interaction analysis showing significant differences in communication pathways between E3-IFI6 and myeloid cells in the ICI-MP-H and ICI-MP-L groups.
(H) Contribution of ligand-receptor pairs for E3-IFI6 (top) and Ma-MHC (bottom).
(I) Comparison of the interaction signal intensity between E3-IFI6 and myeloid subpopulations between the ICI-MP-H and ICI-MP-L groups.
(J) Spatial *in situ* visualization of niches (upper) and expression scores of the antigen-linked interaction module (lower). Scale bars, 10 μm.
(K) The network between the antigen-linked interaction module and the immune inflammation and extracellular matrix (ECM) remodeling modules (identified via InSituCor algorithm).
(L) Multicolor immunofluorescence shows the cross-talk between IFI6+ tumor cells and HLA-DRB+ macrophages via the ligand-receptor pair of APP-CD74. Scale bars, 1 μm.
(M) Univariate analysis of the prognostic impact of E3-IFI6, Ma-MHC, and the combined signature on patient mortality.
(N) Survival analysis of the patients with LUAD from the TCGA cohort based on the combined signature.
Statistical analysis was performed using the Wilcoxon test. $^{*}p < 0.05$, $^{**}p < 0.01$, $^{***}p < 0.001$; ns, no significant difference.

further studies including animal models and organoid-based experiments are still needed to fully delineate the regulatory mechanisms governing downstream protein pathways. These objectives will be the focus of our subsequent research efforts.

RESOURCE AVAILABILITY

Lead contact

Further information and requests for resources and reagents should be directed to and will be fulfilled by the lead contact, Minghui Zhang (zhmhuidoc@163.com).

Materials availability

This study did not generate new unique reagents.

Data and code availability

- Data: Spatial transcriptomics data are accessible in the National Omics Data Encyclopedia (BioProject ID: PRJCA040091). The public data of the NSCLC ICI Immunotherapy cohorts are available in the GEO datasets GEO: GSE126044, GSE135222, and GSE166449. The scRNA-seq data of NSCLC immunotherapy are also available in the GEO dataset GEO: GSE207422.
- Code: This article does not report original code.
- General statement: Any additional information required to reanalyze the data reported in this paper is available from the lead contact upon request.

ACKNOWLEDGMENTS

We sincerely appreciate the invaluable assistance provided by Harbin Medical University Cancer Hospital and the Shenzhen Engineering Center for Translational Medicine of Precision Cancer Immunodiagnosis and Therapy in data collection, data analysis, and other aspects of this study. This work was supported by the Chongqing High-level Medical Talents Project for Young and Middle-aged Professionals (grant no. YXGD202544) and the Technology Innovation Key R&D Program of Chongqing (grant no. CSTB2025TIAD-STX0046).

AUTHOR CONTRIBUTIONS

Conceptualization, H.L. and M.Z.; methodology, H.L., S.L., and N.Q; writing, H.L., S.L., N.Q., J.M., X.L., and M.Z.; review & editing, H.L., S.L., N.Q., J.M., X.L., and M.Z.; funding acquisition, M.Z.; resources, M.Z. and M.Y; investigation, N.Q.; validation, N.Q.; supervision, X.L., L.L., X.Z., L.S., Y.Y., and M.Y.

DECLARATION OF INTERESTS

The authors declare no competing interests.

STAR★METHODS

Detailed methods are provided in the online version of this paper and include the following:

- KEY RESOURCES TABLE
- EXPERIMENTAL MODEL AND STUDY PARTICIPANT DETAILS
  - Human samples
  - Cell lines
- METHOD DETAILS
  - CosMx SMI
  - Sample preparation for SMI
  - Single-cell spatial data generation and quality control
  - Normalization and construction of cell-specific enhancement matrix
  - Data integration and dimension reduction
  - Unsupervised clustering and cell type identification
  - Co-embedding SMI and scRNA-seq datasets
  - Meta-program identification and functional annotation
  - Calculation of the predictive signature score from the validation cohort
  - Differential expression analyses and functional enrichment analyses
  - Gene module enrichment analysis
  - Co-occurrence across spatial dimensions
  - Cell-cell interaction analysis
  - Identification of cell niches
  - Single-cell RNA sequencing data processing and analysis
  - Identification of spatial gene co-expression modules
  - Cox regression analysis
  - Multiplex immunofluorescence (mIF) and quantitative analysis
  - Survival analysis
  - Lentiviral transduction and stable cell line construction
  - Macrophage differentiation and polarization
  - Quantitative real-time PCR (qPCR)
  - Western blotting assay
- QUANTIFICATION AND STATISTICAL ANALYSIS

SUPPLEMENTAL INFORMATION

Supplemental information can be found online at https://doi.org/10.1016/j.xcrm.2026.102760.

Received: May 28, 2025
Revised: October 1, 2025
Accepted: March 23, 2026
Published: April 20, 2026

REFERENCES

1. Thai, A.A., Solomon, B.J., Sequist, L.V., Gainor, J.F., and Heist, R.S. (2021). Lung cancer. Lancet *398*, 535–554. https://doi.org/10.1016/S0140-6736(21)00312-3.
2. Sharma, P., Goswami, S., Raychaudhuri, D., Siddiqui, B.A., Singh, P., Nagarajan, A., Liu, J., Subudhi, S.K., Poon, C., Gant, K.L., et al. (2023). Immune checkpoint therapy-current perspectives and future directions. Cell *186*, 1652–1669. https://doi.org/10.1016/j.cell.2023.03.006.
3. Otano, I., Ucero, A.C., Zugazagoitia, J., and Paz-Ares, L. (2023). At the crossroads of immunotherapy for oncogene-addicted subsets of NSCLC. Nat. Rev. Clin. Oncol. *20*, 143–159. https://doi.org/10.1038/s41571-022-00718-x.
4. Negrao, M.V., Skoulidis, F., Montesion, M., Schulze, K., Bara, I., Shen, V., Xu, H., Hu, S., Sui, D., Elamin, Y.Y., et al. (2021). Oncogene-specific differences in tumor mutational burden, PD-L1 expression, and outcomes from immunotherapy in non-small cell lung cancer. J. Immunother. Cancer *9*, e002891. https://doi.org/10.1136/jitc-2021-002891.
5. Hastings, K., Yu, H.A., Wei, W., Sanchez-Vega, F., DeVeaux, M., Choi, J., Rizvi, H., Lisberg, A., Truini, A., Lydon, C.A., et al. (2019). EGFR mutation subtypes and response to immune checkpoint blockade treatment in non-small-cell lung cancer. Ann. Oncol. *30*, 1311–1320. https://doi.org/10.1093/annonc/mdz141.
6. Lisberg, A., Cummings, A., Goldman, J.W., Bornazyan, K., Reese, N., Wang, T., Coluzzi, P., Ledezma, B., Mendenhall, M., Hunt, J., et al. (2018). A Phase II Study of Pembrolizumab in EGFR-Mutant, PD-L1+, Tyrosine Kinase Inhibitor Naïve Patients With Advanced NSCLC. J. Thorac. Oncol. *13*, 1138–1145. https://doi.org/10.1016/j.jtho.2018.03.035.
7. Skoulidis, F., Byers, L.A., Diao, L., Papadimitrakopoulou, V.A., Tong, P., Izzo, J., Behrens, C., Kadara, H., Parra, E.R., Canales, J.R., et al. (2015). Co-occurring genomic alterations define major subsets of KRAS-mutant lung adenocarcinoma with distinct biology, immune profiles, and therapeutic vulnerabilities. Cancer Discov. *5*, 860–877. https://doi.org/10.1158/2159-8290.CD-14-1236.
8. Dong, Z.-Y., Zhong, W.-Z., Zhang, X.-C., Su, J., Xie, Z., Liu, S.-Y., Tu, H.-Y., Chen, H.-J., Sun, Y.-L., Zhou, Q., et al. (2017). Potential Predictive

Value of TP53 and KRAS Mutation Status for Response to PD-1 Blockade Immunotherapy in Lung Adenocarcinoma. Clin. Cancer Res. *23*, 3012–3024. https://doi.org/10.1158/1078-0432.CCR-16-2554.

9. Harada, G., Yang, S.-R., Cocco, E., and Drilon, A. (2023). Rare molecular subtypes of lung cancer. Nat. Rev. Clin. Oncol. *20*, 229–249. https://doi.org/10.1038/s41571-023-00733-6.
10. Guisier, F., Dubos-Arvis, C., Viñas, F., Doubre, H., Ricordel, C., Ropert, S., Janicot, H., Bernardi, M., Fournel, P., Lamy, R., et al. (2020). Efficacy and Safety of Anti-PD-1 Immunotherapy in Patients With Advanced NSCLC With BRAF, HER2, or MET Mutations or RET Translocation: GFPC 01-2018. J. Thorac. Oncol. *15*, 628–636. https://doi.org/10.1016/j.jtho.2019.12.129.
11. Sabari, J.K., Leonardi, G.C., Shu, C.A., Umeton, R., Montecalvo, J., Ni, A., Chen, R., Dienstag, J., Mrad, C., Bergagnini, I., et al. (2018). PD-L1 expression, tumor mutational burden, and response to immunotherapy in patients with MET exon 14 altered lung cancers. Ann. Oncol. *29*, 2085–2091. https://doi.org/10.1093/annonc/mdy334.
12. Takano, Y., Suzuki, J., Nomura, K., Fujii, G., Zenkoh, J., Kawai, H., Kuze, Y., Kashima, Y., Nagasawa, S., Nakamura, Y., et al. (2024). Spatially resolved gene expression profiling of tumor microenvironment reveals key steps of lung adenocarcinoma development. Nat. Commun. *15*, 10637. https://doi.org/10.1038/s41467-024-54671-7.
13. Yan, Y., Sun, D., Hu, J., Chen, Y., Sun, L., Yu, H., Xiong, Y., Huang, Z., Xia, H., Zhu, X., et al. (2025). Multi-omic profiling highlights factors associated with resistance to immuno-chemotherapy in non-small-cell lung cancer. Nat. Genet. *57*, 126–139. https://doi.org/10.1038/s41588-024-01998-y.
14. Fan, G., Xie, T., Tang, L., Li, L., Han, X., and Shi, Y. (2024). The co-location of CD14+APOE+ cells and MMP7+ tumour cells contributed to worse immunotherapy response in non-small cell lung cancer. Clin. Transl. Med. *14*, e70009. https://doi.org/10.1002/ctm2.70009.
15. Liu, B., Zhang, Y., Wang, D., Hu, X., and Zhang, Z. (2022). Single-cell meta-analyses reveal responses of tumor-reactive CXCL13+ T cells to immune-checkpoint blockade. Nat. Cancer *3*, 1123–1136. https://doi.org/10.1038/s43018-022-00433-7.
16. Bassez, A., Vos, H., Van Dyck, L., Floris, G., Arijs, I., Desmedt, C., Boeckx, B., Vanden Bempt, M., Nevelsteen, I., Lambein, K., et al. (2021). A single-cell map of intratumoral changes during anti-PD1 treatment of patients with breast cancer. Nat. Med. *27*, 820–832. https://doi.org/10.1038/s41591-021-01323-8.
17. Singhal, V., Chou, N., Lee, J., Yue, Y., Liu, J., Chock, W.K., Lin, L., Chang, Y.-C., Teo, E.M.L., Aow, J., et al. (2024). BANKSY unifies cell typing and tissue domain segmentation for scalable spatial omics data analysis. Nat. Genet. *56*, 431–441. https://doi.org/10.1038/s41588-024-01664-3.
18. Tyler, M., Gavish, A., Barbolin, C., Tschernichovsky, R., Hoefflin, R., Mints, M., Puram, S.V., and Tirosh, I. (2025). The Curated Cancer Cell Atlas provides a comprehensive characterization of tumors at single-cell resolution. Nat. Cancer *6*, 1088–1101. https://doi.org/10.1038/s43018-025-00957-8.
19. Chan, J.M., Quintanal-Villalonga, Á., Gao, V.R., Xie, Y., Allaj, V., Chaudhary, O., Masilionis, I., Egger, J., Chow, A., Walle, T., et al. (2021). Signatures of plasticity, metastasis, and immunosuppression in an atlas of human small cell lung cancer. Cancer Cell *39*, 1479–1496.e18. https://doi.org/10.1016/j.ccell.2021.09.008.
20. Hu, J., Zhang, L., Xia, H., Yan, Y., Zhu, X., Sun, F., Sun, L., Li, S., Li, D., Wang, J., et al. (2023). Tumor microenvironment remodeling after neoadjuvant immunotherapy in non-small cell lung cancer revealed by single-cell RNA sequencing. Genome Med. *15*, 14. https://doi.org/10.1186/s13073-023-01164-9.
21. Danaher, P., McGuire, D., Wu, L., Patrick, M., Kroeppler, D., Zhai, H., Olgun, D.G., Gong, D., Cao, J., Hwang, W.L., et al. (2025). InSituCor: exploring spatially correlated genes conditional on the cell type landscape. Genome Biol. *26*, 105. https://doi.org/10.1186/s13059-025-03554-1.
22. Brahmer, J., Reckamp, K.L., Baas, P., Crinò, L., Eberhardt, W.E.E., Poddubskaya, E., Antonia, S., Pluzanski, A., Vokes, E.E., Holgado, E., et al. (2015). Nivolumab versus Docetaxel in Advanced Squamous-Cell Non-Small-Cell Lung Cancer. N. Engl. J. Med. *373*, 123–135. https://doi.org/10.1056/NEJMoa1504627.
23. Mazieres, J., Drilon, A., Lusque, A., Mhanna, L., Cortot, A.B., Mezquita, L., Thai, A.A., Mascaux, C., Couraud, S., Veillon, R., et al. (2019). Immune checkpoint inhibitors for patients with advanced lung cancer and oncogenic driver alterations: results from the IMMUNOTARGET registry. Ann. Oncol. *30*, 1321–1328. https://doi.org/10.1093/annonc/mdz167.
24. Offin, M., Guo, R., Wu, S.L., Sabari, J., Land, J.D., Ni, A., Montecalvo, J., Halpenny, D.F., Buie, L.W., Pak, T., et al. (2019). Immunophenotype and Response to Immunotherapy of RET-Rearranged Lung Cancers. JCO Precis. Oncol. *3*, PO.18.00386. https://doi.org/10.1200/PO.18.00386.
25. Hanna, N.H., Schneider, B.J., Temin, S., Baker, S., Brahmer, J., Ellis, P.M., Gaspar, L.E., Haddad, R.Y., Hesketh, P.J., Jain, D., et al. (2020). Therapy for Stage IV Non-Small-Cell Lung Cancer Without Driver Alterations: ASCO and OH (CCO) Joint Guideline Update. J. Clin. Oncol. *38*, 1608–1632. https://doi.org/10.1200/JCO.19.03022.
26. Stuart, T., Butler, A., Hoffman, P., Hafemeister, C., Papalexi, E., Mauck, W.M., Hao, Y., Stoeckius, M., Smibert, P., and Satija, R. (2019). Comprehensive Integration of Single-Cell Data. Cell *177*, 1888–1902.e21. https://doi.org/10.1016/j.cell.2019.05.031.
27. Ito, K., and Murphy, D. (2013). Application of ggplot2 to Pharmacometric Graphics. CPT Pharmacometrics Syst. Pharmacol. *2*, e79. https://doi.org/10.1038/psp.2013.56.
28. Zeng, D., Fang, Y., Qiu, W., Luo, P., Wang, S., Shen, R., Gu, W., Huang, X., Mao, Q., Wang, G., et al. (2024). Enhancing immuno-oncology investigations through multidimensional decoding of tumor microenvironment with IOBR 2.0. Cell Rep. Methods *4*, 100910. https://doi.org/10.1016/j.crmeth.2024.100910.
29. Korsunsky, I., Millard, N., Fan, J., Slowikowski, K., Zhang, F., Wei, K., Baglaenko, Y., Brenner, M., Loh, P.R., and Raychaudhuri, S. (2019). Fast, sensitive, and accurate integration of single cell data with Harmony. Nat. Methods *16*, 1289–1296. https://doi.org/10.1038/s41592-019-0619-0.
30. S, J., Mv, P., and Q, N. (2025). CellChat for systematic analysis of cell-cell communication from single-cell transcriptomics. Nat. Protoc. *20*, 180. https://doi.org/10.1038/s41596-024-01045-4.
31. Franzén, O., Gan, L.-M., and Björkegren, J.L.M. (2019). PanglaoDB: a web server for exploration of mouse and human single-cell RNA sequencing data. Database *2019*, baz046. https://doi.org/10.1093/database/baz046.
32. Palla, G., Spitzer, H., Klein, M., Fischer, D., Schaar, A.C., Kuemmerle, L.B., Rybakov, S., Ibarra, I.L., Holmberg, O., Virshup, I., et al. (2022). Squidpy: a scalable framework for spatial omics analysis. Nat. Methods *19*, 171–178. https://doi.org/10.1038/s41592-021-01358-2.

STAR★METHODS

KEY RESOURCES TABLE

REAGENT or RESOURCE	SOURCE	IDENTIFIER
Antibodies		
Anti human DAPI (for SMI detection)	Nanostring	Cat# 20250326
Anti human CD298 (for SMI detection)	Nanostring	Cat# 250521–01; RRID : AB_3720478
Anti human PanCK (for SMI detection)	Nanostring	Cat# 250327–01: RRID : AB_2935724
Anti human CD45 (for SMI detection)	Nanostring	Cat# 250327–01: RRID : AB_2935724
Anti human CD68 (for SMI detection)	Nanostring	Cat# 251021–02: RRID : AB_2893077
Anti human PanCK (for additional mIF validation)	ZhongShang JinQiao	Cat# ZM-0069: RRID:AB_2941997
Anti human IFI6 (for additional mIF validation)	Beijing Bioasen	Cat# BS-15552R
Anti human APP (for additional mIF validation)	Protein tech	Cat# 60342-1-IG: RRID:AB_2881451
Anti human CD68 (for additional mIF validation)	Gene Technology (Shanghai)	Cat# GM087629
Anti human HLA-DRB (for additional mIF validation)	Abcam	Cat# ab92511: RRID:AB_10563656
Anti human CD74 (for additional mIF validation)	Abcam	Cat# AB108393: RRID:AB_10859956
Anti rabbit IFI6 (for experimental validation)	CST	Cat# 71578T
Anti rabbit GAPDH (for experimental validation)	Abclonal	Cat# A19056: RRID:AB_2862549
Anti rabbit IgG (for experimental validation)	Abclonal	Cat# AS014: RRID:AB_2769854
Chemicals, peptides, and recombinant proteins		
Digestion buffer	Vazyme	Cat# GMP4302R-00
NHS-acetate	Thermo	Cat# 26777
Absolute ethanol (100% ethanol)	Thermo	Cat# 033361.M1
DEPC water	Beyotime	Cat# R0021
Antigen retrieval buffer	Abcam	Cat# AB93684
Critical commercial assays		
cDNA Synthesis Kit	Zsgene	Cat# ZS-M14003
SYBR green qPCR reagent	Zsgene	Cat# ZS-M13002
Cell lines and media		
Human: HEK293T cell line	Procell	CL-0005
NCI-H1975	Procell	CL-0298
NCI-H23	Procell	CL-0397
THP-1	Procell	CL-0233
HEK-293T cell Complete Medium	Procell	CM-0005
NCI-H1975 Cell Complete Medium	Procell	CM-0298
NCI-H23 Cell Complete Medium	Procell	CM-0397
THP-1 Cell Complete Medium	Procell	CM-0233
ACCUTASE	YEASEN	Cat# 40506ES60
Primers		
qPCR Primers for CD86, TNF-α, IL-12, HLA-DRB, CD206, CD163, Arg1, TGF-β, ACTB	Zsgene	N/A
Deposited data		
The original RDS files	This paper	NODE: https://ngdc.cncb.ac.cn/bioproject/browse/PRJCA04009
NSCLC ICI Immunotherapy cohorts	Gene Expression Omnibus (GEO)	GEO: GSE126044, GSE135222, GSE166449
NSCLC Single-Cell Reference Data	3CA database[18]	https://www.weizmann.ac.il/sites/3CA
NSCLC Immunotherapy Single-Cell Data	Gene Expression Omnibus (GEO)[20]	GEO: GSE207422

(*Continued on next page*)

Continued

REAGENT or RESOURCE	SOURCE	IDENTIFIER
GDC TCGA LUAD Lung Adenocarcinoma (LUAD) cohort	Xena database	https://xenabrowser.net/datapages/
TCGA LUAD Lung Adenocarcinoma (LUAD) cohort	Xena database	https://xenabrowser.net/datapages/
Software and algorithms		
R (v4.0.0)		https://www.rproject.org
Seurat (v3.2.2)	Hao et al.[26]	https://satijalab.org/seurat/
ggplot2 (v3.5.2)	Pedersen et al.[27]	https://tidyverse.r-universe.dev/ggplot2
CellChat (v1.6.1)	Jin et al.	https://github.com/sqjin/CellChat
IOBR (v0.99.0)	Zeng, D. et al.[28]	https://github.com/IOBR/IOBR
Banksy (v0.99.12)	Singhal, V. et al.[17]	https://github.com/prabhakarlab/Banksy
survminer (v0.5.2)	Kassambara et al.	https://github.com/kassambara/survminer
survival (v3.8-3)	Therneau et al.	https://cran.rproject.org/web/packages/survival/index.html
InSituCor(v0.0.0.9000)	Danaher, P et al.[21]	https://github.com/Nanostring-Biostats/InSituCor
harmony (v1.2.1)	Korsunsky, I. et al.[29]	https://github.com/immunogenomics/harmony

EXPERIMENTAL MODEL AND STUDY PARTICIPANT DETAILS

Human samples

We selected 38 tumor tissue samples from patients with LUAD at Harbin Medical University Cancer Hospital between January 2021 and January 2024. Inclusion criteria were as follows: (1) histopathologically confirmed newly diagnosed lung adenocarcinoma (LUAD) within non-small cell lung cancer (NSCLC); (2) patient age between 20 and 90 years; (3) presence of rare oncogenic driver mutations with available targeted therapeutic agents; and (4) normal hepatic, renal, and hematologic function. Exclusion criteria were: (1) patients with incomplete or missing clinical information; and (2) patients with SARS-CoV-2 infection. A total of 38 LUAD patients were enrolled in this study. Tissue specimens were obtained from patients before the initiation of treatment. All specimens were fixed in formalin, embedded in paraffin (FFPE), and sequentially sliced into 5-μm-thick sections. H&E staining was performed on the paraffin-embedded tissue sections to confirm the diagnosis, assess tissue quality, and determine tumor content, all evaluated by an experienced thoracic pathologist. Of the 38 patients, 36 harbored nine distinct types of driver-gene mutations, whereas the remaining 2 showed no significant driver-gene alterations. Clinical information of all the patients is provided in Table S1. The study was approved by the Ethics Committee of Harbin Medical University Cancer Hospital (approval no. YD2025-15), and all patients provided written informed consent prior to participation.

Cell lines

The human lung adenocarcinoma cell lines (NCI-H1975 and NCI-H23), the human monocytic cell line THP-1 and the human embryonic kidney cells HEK293T were obtained from Procell Life Science & Technology (Procell). All cells were cultured in complete medium (Procell) supplemented with 10% fetal bovine serum (FBS) and 1% penicillin-streptomycin. Cells were maintained in a humidified incubator (Thermo Scientific) at 37°C with 5% CO2. Cell lines used in this study were tested for mycoplasma contamination and authenticated by STR profiling.

METHOD DETAILS

CosMx SMI

CosMx technology [CosMx Human Universal Cell Characterization RNA Panel (1000-plex); NanoString, USA] was used for 38 FFPE samples. An average of 9 fields of view (FOVs) were analyzed per sample (total of 372 FOVs). The average explored area was 1.35mm^2 per sample. The following cell surface markers were used for morphological visualization: CD298, PanCK/D45, CD68 antibodies, and DAPI.

Sample preparation for SMI

Tissue preparation for SMI and RNA assay was performed in accordance with the manufacturer's instructions. Briefly, FFPE TMA tissue slide was baked overnight at 60°C to ensure adherence of the charged glass slides. Tissue preparation followed the CosMx SMI slide preparation manual (MAN-10184-02). To expose target RNAs and epitopes, the tissues underwent deparaffinization in xylene, heat-induced epitope retrieval (HIER) using Citrate Buffer (pH 6.0) at 100°C for 15min, and enzymatic permeabilization with 3μg/ml digestion buffer at 40°C for 30min. Subsequently, a 0.0005% working concentration of fiducials was applied to facilitate coordinate alignment, followed by post-fixation with 10% neutral buffered formalin and blocking using NHS-acetate. For RNA

detection, an overnight hybridization at 37°C was performed using the CosMx universal cell characterization 1000 plex RNA panel (#121500041, NanoString Technologies) of probes. The next day, the tissues were subjected to stringent washes (2× SSC/50% formamide) to eliminate any unbound probe. To define cell boundaries and tissue architecture, protein-level mIF staining was performed using a cocktail of morphology markers, including DAPI for nuclear staining, along with fluorescently conjugated antibodies against CD298, PanCK/CD45, and CD68. The prepared slide was then assembled into a fluidic manifold to form a flow cell and loaded onto the SMI instrument. The imaging run was set up using the standard 60s FOV pre-bleaching profile and automated cell segmentation profile for human tissue to ensure high-quality *in-situ* analyte readout.

Single-cell spatial data generation and quality control

The original RDS files were exported using the SMI AtoMx platform, and subsequent analysis was conducted by the Seurat package (version 5.1.0)[26] in R software (version 4.0.0). For each sample, cells with issues, such as tissue detachment, fluorescence overexposure, or poor quality, were excluded. Quality control was performed for each cell based on three criteria, and the cells were excluded if they met any of the following conditions: (1) fewer than 10 expressed genes, (2) fewer than 20 detected features, or (3) detected features exceeding the upper limit (defined as the top 98% of all cells by the number of detected features). To minimize data contamination resulting from cell boundary ambiguities during cell separation (which could lead to multiple cells being classified as a single cell), doublets were detected and removed using the scDblFinder package (version 0.2.1), with all parameters set to default.

Normalization and construction of cell-specific enhancement matrix

The gene expression matrix was normalized using the NormalizeData function, with the ''normalization.method'' parameter set to ''RC'' and the ''scale.factor'' set to the median of ''nFeature_RNA.'' All 1000 genes were used as variable features in the subsequent analysis. The RunBanksy function from the Banksy package (version 0.99.12) in R was used to integrate the cell expression matrix with its spatial coordinate information, generating an enhanced matrix that includes the spatial features of the cells. The parameters were set as follows: lambda = 0.2, k_geom = 15, features = 'all', and group = 'sample'. The integrated enhanced matrix was used exclusively for dimensionality reduction and clustering. Differential expression and gene set analyses were conducted using data normalized from the raw gene expression matrix.

Data integration and dimension reduction

PCA was performed on the integrated enhanced matrix using the RunPCA function. The top 20 principal components (PCs) were selected based on the elbow plot and used as the input for subsequent analysis. The data were then corrected using the RunHarmony function from the harmony package (version 1.2.1) with the parameter group.by.vars = 'sample', After correction, Uniform Manifold Approximation and Projection (UMAP) was performed using the RunUMAP function, with visualization in a two-dimensional space.

Unsupervised clustering and cell type identification

We used the harmony-integrated data as input for the FindNeighbors function. The resolution parameter for the FindClusters function varied for different cell types; a resolution of 0.6 was used for all cells, 0.4 was used for myeloid cells, and 0.3 was used for epithelial cells. Cell type annotations were based on classic marker genes, with marker genes for each cluster identified by the FindAllMarkers function, using all default parameters. Differentially expressed genes (DEGs) were determined by performing the Wilcoxon rank-sum test on the samples, with the following filtering criteria: p-value <0.05, average $|\log_2$ fold change$| > 0.5$, and pct.2 < 0.5. Cell type marker genes were referenced from the CellMarker[30] and PanglaoDB[31] databases.

Co-embedding SMI and scRNA-seq datasets

A reference single-cell atlas was generated to validate the accuracy of cell type annotations. scRNA-seq data from Chan et al., 2021[19] were downloaded from the 3CA database (https://www.weizmann.ac.il/sites/3CA/). The reference scRNA dataset was co-embedded with the SMI data through reciprocal PCA. For each dataset, integration was first performed based on the 20 most optimal anchors, followed by integration using the top 30 PCs from each dataset. This process was implemented using the Seurat R package (version 5.1.0). The co-embedded data were then visualized using two-dimensional UMAP. A detailed description of the co-embedding pipeline is available in Seurat's tutorials (https://satijalab.org/seurat/articles/integration_rpca.html).

Meta-program identification and functional annotation

We analyzed the gene expression data from 38 LUAD samples. cNMF analysis was performed on all cells (nprograms = 20) and on epithelial cells (nprograms = 15) using the GeneNMF package (version 0.4.0) in R. The multimf function was applied across different values of k, ranging from 6 to 9, resulting in the identification of 16 MPs in all cells and 9 E-MPs in epithelial cells. To ensure the accuracy of the analysis, we further removed redundant or low-quality MPs (defined as MPs with three or fewer genes in the gene list), ultimately retaining 13 MPs (Table S3) and 5 E-MPs. MP score for each cell was calculated using the AddModuleScore_UCell function. To further characterize the biological processes represented by the identified MPs and E-MPs, we downloaded summarized MP signature collections from the 3CA database, including malignant cell, epithelial cell, and TME-derived signatures (covering T/B cells,

fibroblasts, endothelial cells, and myeloid cells), as a reference. We then systematically compared the genes contained in each identified MP signature with those in the reference signatures, quantified the number of overlapping genes for each MP, and subsequently annotated the identified MPs based on these overlaps.

Calculation of the predictive signature score from the validation cohort

The gene expression matrices of 65 patients with NSCLC receiving ICI therapy were downloaded from the Gene Expression Omnibus (GEO: GSE126044, GSE135222, and GSE166449). Notably, the NSCLC subtypes of these patients were neither mentioned nor specifically distinguished in the original study. Signature scores for different MPs were calculated for each patient using the calculate_sig_score function from the package IOBR (version 0.99.0), with all parameters set to default. After calculating the signature score for each individual patient, differences in each MP signature score between the ICI-responsive (RE) and non-responsive (NRE) groups were assessed using the stat_compare_means function from the ggpubr R package (version 0.6.0), treating each patient as an independent data point. Statistical significance was determined using the Wilcoxon rank-sum test, and MPs with p-values $\leq$0.05 (MP2, MP9, MP16, and MP17) were considered significantly associated with response. Then, the MP2, MP9, MP16, and MP17 scores for each mutation type were first subjected to Z score standardization to ensure comparability. Subsequently, inter-group dissimilarity was quantified by calculating the Canberra distance. Finally, hierarchical clustering was performed using the Ward.D linkage method to minimize within-cluster variance and identify distinct clusters of mutation types characterized by convergent MP profiles.

Differential expression analyses and functional enrichment analyses

Differential expression analysis of epithelial cells between the ICI-MP-H and ICI-MP-L groups was performed using the FindMarkers function, with parameters set to "min.pct = 0.1" and "thresh.use = 0.25." Gene Ontology (GO) enrichment analysis was conducted using the clusterProfiler package in R. GO terms with adjusted p-values <0.05 were considered statistically significant.

Gene module enrichment analysis

To assess the characteristics of epithelial cell subpopulations, we calculated pathway enrichment scores for each cell using the AddModuleScore function in Seurat, based on gene lists corresponding to various biological pathways provided by the SMI AtoMx platform.

Co-occurrence across spatial dimensions

To quantify the spatial relationships across different cell types within a given sample, we used the Squidpy Python package to calculate the distribution of each cell type across different samples. For each sample, the cell neighbor matrix was first constructed using the sq.gr.spatial_neighbors function with n_neighs set to 10. Next, the sq.gr.co_occurrence function was applied with default parameters to calculate the cooccurrence probabilities between a given cell type and all other cell types at various spatial distances. Only cell types with a cell count of >10 were analyzed. For each sample, the average co-occurrence probabilities for the top 5 closest distances were taken as the co-occurrence score between two cell types. Detailed information can be found in the Squidpy publication in *Nature Methods*.[32]

Cell-cell interaction analysis

We used CellChat (version 1.6.1) to infer cell–cell interactions between different cell types.[30] Significant interactions were identified using a trimean thresholding approach. During the analysis, the netVisual_circle function was used to visualize the intensity of the cell–cell communication network from target cell populations to various other cell groups. The computeCommunProb function was employed to assess the communication probabilities. The netAnalysis_contribution function was used to calculate the contribution of each ligand–receptor pair to the overall signaling pathway. Finally, the 'netVisual_bubble' tool was used to graphically display significant ligand–receptor interactions between the cells of interest.

Identification of cell niches

Compared to traditional scRNA-seq, spatial single-cell transcriptomics includes additional spatial coordinate information for each cell. Therefore, we performed cell ecological niche analysis using the Banksy package (version 0.99.12) in R. The steps for region classification were as follows: first, an enhanced matrix of all cells was constructed (with the lambda parameter set to 0.8 during matrix construction). PCA was applied for dimensionality reduction, and harmony was used to correct for batch effects and integrate the data. Next, UMAP was used for further dimensionality reduction and visualization. The number of clusters with a final resolution of 0.1 was used for subsequent analysis.

Single-cell RNA sequencing data processing and analysis

Raw single-cell RNA sequencing (scRNA-seq) data from lung adenocarcinoma (LUAD) patients undergoing immunotherapy were obtained from the GEO database GEO: GSE207422. Expression matrices were integrated with patient clinical information using the CreateSeuratObject function to generate a Seurat object for downstream analysis. scRNA-seq data were processed following the original study's pipeline to closely reproduce the published results. Data normalization was performed using default parameters,

and the top 3,000 highly variable genes were selected for downstream analysis. Batch correction across samples was performed using Harmony based on the sample metadata. The top 20 principal components (PCs) were used as input for subsequent analyses. Clustering was conducted with a resolution of 0.3. Differentially expressed genes were identified using the FindAllMarkers function, and cell-type annotation was performed based on canonical marker genes from CellMarker and as described in the original study.

Identification of spatial gene co-expression modules

To identify gene co-expression modules independent of cell types within individual samples, we employed the InSituCor package (version 0.0.0.9000) in R. The input data included the gene expression matrix and the spatial coordinates (X, Y) of each cell. The insituco function was applied with the following key parameters: resolution = 0.02, k = 100, min_module_size = 5, max_module_size = 100, min_module_cor = 0.05, and roundcortozero = 0.1, while other parameters were kept as default. This step generated the spatial correlation condition matrix, from which gene modules were subsequently derived. The module scores were visualized *in situ* using the built-in function plot(xy.tmp). In addition, inter-module correlations were assessed and visualized as clustering networks using the plotCorrelationNetwork function.

Cox regression analysis

RNA-seq data with corresponding survival information from LUAD patients (TCGA LUAD cohort) were downloaded from the Xena database. Patients with missing overall survival time or survival status were excluded, resulting in a final cohort of 632 patients. Signature scores for each patient, including E3-IFI6-signature, Ma-MHC-signature, and combined signature, were calculated using the IOBR package (version 0.99.0). Cox proportional hazards regression analysis was performed using the coxph function, including three variables in the model: E3-IFI6-signature, Ma-MHC-signature, and combined signature. Forest plots displaying hazard ratios (HRs) and 95% confidence intervals (CIs) were generated using ggforest from the package survminer (version 0.5.2). Additional visualization of regression coefficients was performed with forest_model and ggcoef_model from the package ggstats (version 0.9.0), with point shapes indicating statistical significance, allowing intuitive assessment of the impact of each meta-program on patient survival.

Multiplex immunofluorescence (mIF) and quantitative analysis

FFPE tissue sections were processed for multiplex immunofluorescence (mIF) staining as follows. Sections were deparaffinized in xylene (10min $\times$ 3), followed by rehydration through a graded ethanol series (100%, 90%, 70%, 5 min each) and rinsed in distilled water for 3min. Antigen retrieval was performed by immersing the slides in antigen retrieval buffer and heating in a microwave: high power to boiling, followed by low power for 15min. Slides were allowed to cool naturally and washed with TBST three times (3min each). Endogenous peroxidase activity was blocked by incubating the sections with 3% hydrogen peroxide for 10min at room temperature in the dark, followed by three washes in TBST (3min each). Non-specific binding sites were blocked with goat serum for 30min at room temperature. Primary antibodies were applied to the sections in the order specified in the staining protocol and incubated for 1h in a humidified chamber, followed by three washes in TBST (5min each). Secondary antibodies were then applied for 10min at room temperature, followed by three washes in TBST (5min each). Fluorescent dyes were subsequently applied according to the staining protocol and incubated for 10min, with three TBST washes (5min each). Steps of antigen retrieval, primary/secondary antibody incubation, and fluorescent dye application were repeated sequentially for all markers as specified in the staining protocol. Nuclear counterstaining was performed with DAPI for 10min at room temperature, followed by three TBST washes (3min each). Slides were then mounted with antifade mounting medium. Images were acquired using a PANNORAMIC SCAN II Imaging System (3DHistech, Hungary).

Survival analysis

Bulk RNA-seq data were obtained from the UCSC Xena database (https://xenabrowser.net/datapages/), specifically from the GDC TCGA LUAD cohort and the TCGA LUAD cohort. The TCGA LUAD dataset was used to evaluate the prognostic significance of gene sets derived from the E3-IFI6 and Ma-MHC clusters. Feature genes for the epithelial and myeloid subpopulations were identified using the FindAllMarkers() function, with the following parameters: average $|\log_2$ fold change$| > 0.5$, adjusted p-value <0.05, pct.1 > 0.2, and pct.2 < 0.5. Based on these results, we selected the feature genes for the E3-IFI6 and Ma-MHC clusters, referred to as E3-IFI6-sig and Ma-sig, respectively. The intersection of these two signatures was defined as an integrated signature, termed common-sig. Survival analysis was conducted using the Cox proportional hazards model implemented in the survival package in R (version 3.8-3). Forest plots were generated using the ggcoef_model() function from the ggstatsplot package (version 3.2.2), and Kaplan–Meier survival curves were plotted using the ggsurvplot() function from the survminer package (version 0.5.2).

Lentiviral transduction and stable cell line construction

To overexpress IFI6, the human IFI6 ORF was cloned into the pLVX-Puro lentiviral vector. Lentiviral particles were produced by co-transfecting HEK-293T cells with the IFI6 expression plasmid and packaging plasmids (psPAX2 and pMD2.G) using Lipofectamine 2000 (Invitrogen). Target cells (NCI-H1975 and NCI-H23) were transduced with lentiviral supernatants in the presence of 8 μg/mL polybrene. Stable transductants were selected with 1 μg/mL puromycin for 14 days. The overexpression efficiency was confirmed by quantitative real-time PCR (qPCR) and western blotting.

Macrophage differentiation and polarization

THP-1 monocytes were differentiated into M0 macrophages by incubation with 100 ng/mL phorbol 12-myristate 13-acetate (PMA; MCE) for 24h, followed by a 24h rest period in fresh medium. For polarization studies, Transwell inserts (0.4μm pore size; Corning) were used to establish a co-culture system with IFI6-overexpressing or control tumor cells.

Quantitative real-time PCR (qPCR)

Total RNA was extracted using TRIzol reagent (Invitrogen) and reverse-transcribed into cDNA using the Super Brilliant cDNA Synthesis Kit (Zsgene, China). qPCR was performed using Super Brilliant SYBR Green Master Mix (Zsgene, China) on an ABI 7500 Real-Time PCR System. Target gene expression was normalized to *ACTB* using the $2-\Delta\Delta Ct$ method. The primer sequences used in this study are detailed in Table S6.

Western blotting assay

Cells were homogenized in ice-cold RIPA lysis buffer, resolved using 12% SDS-PAGE, and transferred onto polyvinylidene fluoride membranes. After blocking with 5% non-fat milk, the membranes were probed with the following primary antibodies at 4°C overnight: IFI6 (71578T, CST), GAPDH (A19056, Abclonal). The membranes were then incubated with anti-rabbit (AS014, Abclonal) antibody at room temperature for 1h. Images were captured after reaction with the ECL reagent (Millipore, USA).

QUANTIFICATION AND STATISTICAL ANALYSIS

Details of the statistical tests and the sample size n (representing the number of patients) used in each analysis are provided in the corresponding figure legends. For normally distributed data, a two-sided paired *t* test was performed for paired group comparisons. For non-normally distributed data, a two-sided unpaired Wilcoxon test was conducted for independent group comparisons. For differential gene expression analyses, *p*-values were adjusted for multiple testing using the Benjamini–Hochberg method (FDR correction). For the experimental section, statistical analysis was performed using GraphPad Prism. All experimental data are expressed as the mean ± SD of at least three independent biological replicates. Differences between two groups were analyzed using two-tailed Student's t-tests. For comparisons among multiple groups, one-way ANOVA followed by Tukey's post-hoc test was employed. Significant levels are indicated as $^{*}p < 0.05$, $^{**}p < 0.01$, $^{***}p < 0.001$, $^{****}p < 0.0001$.